Journal of Inorganic Biochemistry 199 (2019) 110757

Contents lists available at ScienceDirect

Journal of Inorganic Biochemistry

journal homepage: www.elsevier.com/locate/jinorgbio

Triphenylamine-appended cyclometallated iridium(III) complexes: Preparation, photophysical properties and application in biology/luminescence imaging

Xicheng Liu[a,*], Hailong Hao[a], Xingxing Ge[a], Xiangdong He[a], Yifei Liu[b], Yan Wang[a], Haojie Wang[a], Mingxiao Shao[a], Zhihong Jing[a], Laijin Tian[a], Zhe Liu[a,*]

[a] Institute of Anticancer Agents Development and Theranostic Application, The Key Laboratory of Life-Organic Analysis and Key Laboratory of Pharmaceutical Intermediates and Analysis of Natural Medicine, School of Chemistry and Chemical Engineering, Qufu Normal University, Qufu 273165, China
[b] Qufu Normal University, School of Life Science, Qufu 273165, China

ARTICLE INFO

Keywords:
Triphenylamine
Cyclometallated iridium complex
Photophysical property
Bioactivity
Luminescence imaging

ABSTRACT

Four triphenylamine (TPA)-appended cyclometallated iridium(III) complexes were designed and synthesized. Photophysical properties of these complexes were studied, and density functional theory (DFT) was utilized to analyze the influence of the ancillary ligands (TPA-modified bipyridine) to these complexes. The introduction of TPA units could effectively adjust the lipid solubility of complexes (*logP*), and endowed complexes with potential bioactivity (anticancer, antibacterial and bactericidal activity), especially in the field of anticancer (the best value of IC_{50} is 4.34 ± 0.01 μM). Interestingly, complexe **4** show some selectivity for cancer cells versus normal cells. Meanwhile, complexes could effectively prevent the metastasis of cancer cells. Complexes can be transported by serum albumin and followed by the static quenching mechanism (K_q: 10^{13} M^{-1} s^{-1}), disturb cell cycle at G_0/G_1 phase, and induce apoptosis. The favorable fluorescence property confirmed these complexes followed by an energy-dependent cellular uptake mechanism, effectively accumulated in lysosomes (PCC: > 0.95) and induced lysosomal damage, and eventually leaded to cell death. Our study demonstrates that these complexes are potential anticancer agents with dual functions, including metastasis inhibition and lysosomal damage.

1. Introduction

Iridium(III) (Ir^{III}) complexes have recently emerged as promising alternatives to platinum-based organometallic anticancer drugs because of their unique anticancer mechanisms, e.g., involvement in cellular redox reactions, inhibition of multiple protein activities and protein-protein interactions. [1–4] Among these, cyclometalated complexes provide excellent luminescence properties, e.g., large Stokes shifts, high quantum yields and variable absorption/emission wavelength, thus they have been widely used as biological imaging and fluorescence probes. [5–8] The general formula of cyclometallated Ir^{III} complexes can be expressed as $[Ir(ppy)_2(biPy)]PF_6$, wherein ppy is 2-phenylpyridine or its derivatives (CˆN chelating ligands) and biPy is bipyridine or its derivatives (CˆN chelating ligands). Due to the easy modification of these ligands, the luminescence and biological properties of cyclometallated Ir^{III} complexes can be readily adjusted. [9–11] More importantly, the combination of potential anticancer activity and luminescence properties of cyclometallated Ir^{III} complex makes it possible for the construction of novel theranostic platforms.

Lysosomes are often described as the stomachs of the cells (pH: 4.5–5.5), which contain a variety of hydrolytic enzymes that are capable of degrading almost all kinds of biomacromolecules delivered by ways of phagocytosis, autophagy, and endocytosis. [12,13] In addition, lysosome plays a significant role in intracellular transport, cell migration, metabolism, plasma membrane repair, and even apoptosis. [14,15] Lysosomal dysfunction, a process known as lysosomal membrane permeabilization, can lead to the release of cathepsins and other hydrolases from the lysosomal lumen to the cytosol, thus induce apoptosis. Therefore, lysosomes are emerging as attractive targets for selective killing of cancer cells. Due to the significant acidic environment in the lysosomes of cancer cells, a large number of groups (benzimidazole [16], morpholine [17], rhodamine [18] etc.) or ligands (β-carboline [19], imine-*N*-heterocyclic carbene [20], 2-naphthalen-1-yl-1H-benzoimidazole [21], etc.) containing free electron pairs have been introduced into cyclometallated Ir^{III} complex as lysosomal targeted and real-time tracking drugs, and achieved the ideal results.

* Corresponding authors.
E-mail addresses: chemlxc@163.com (X. Liu), liuzheqd@163.com (Z. Liu).

https://doi.org/10.1016/j.jinorgbio.2019.110757
Received 30 March 2019; Received in revised form 18 June 2019; Accepted 25 June 2019
Available online 27 June 2019
0162-0134/

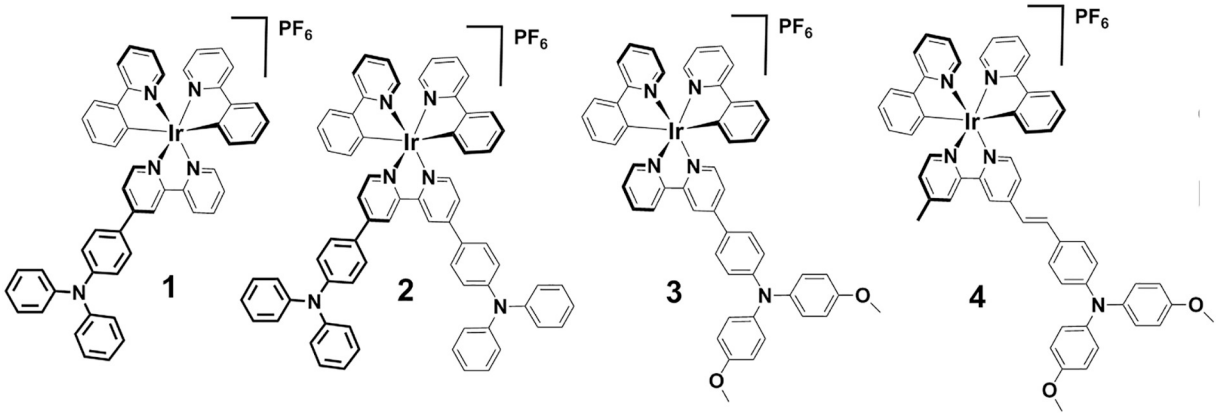

Fig. 1. Structures of designed cyclometalated Ir^{III} complexes.

Triphenylamine (TPA) and its derivatives, hole-transporting and emitting materials, are widely used in organic photoelectric field, e.g., organic light-emitting diodes (OLEDs) [22], organic field effect transistors (OFETs) [23] and perovskite solar cells (PSCs) [24–26]. Recent studies showed that possessed a promising application in biological probes and drug targeting fields due to the advantages of low excitation energy, small light damage and strong penetrability etc. [27–30] TPA-appended phenanthroline chelating ligand (N^N) applied to cyclometallated Ir^{III} complex and acted as an effective phototherapy drug towards HeLa cells, which can effectively induce the production of singlet oxygen ($1O_2$) after 730 nm laser irradiation and lead to apoptosis. [31] Our previous studies also confirmed that half-sandwich iridium(III) complexes with TPA-substituted dipyridine frameworks showed potential anticancer activity and unique anticancer mechanism different from *cis*-platinum [32]. Inspired by above studies, four cyclometallated Ir^{III} complexes ($[Ir(ppy)_2(N^N)]PF_6$) with TPA-appended bipyridine chelating ligands (N^N) and phenylpyridine (ppy) ligands were synthesized and characterized (Fig. 1). The anticancer and antibacterial activity of target complexes towards A549 (human lung cancer) cells and *E. coli* (*Escherichia coli*) were determined by the MTT (3-(4,5-dimethylthiazol-2-yl)-2,5-diphenyltetrazolium bromide) and microcalorimetry assay, respectively. Because of the potential applications in the field of anticancer, the selectivity between normal human cells and tumor cells, the transport and anticancer mechanism of target complexes were also studied. Due to the favorable fluorescent properties of these complexes (the comparison and interpretation were also carried out by means of quantum chemical simulation), laser confocal technology was used to investigate the cellular uptake and target sites in cells. Above all, TPA-modified cyclometallated Ir^{III} complexes are distinguished significative for further evaluation as anticancer drugs.

2. Results and discussion

Triphenylamine-appended cyclometalated Ir^{III} complexes were synthesized by the reaction of $[(ppy)_2IrCl]_2$ (Dimer) and TPA-modified bipyridine (TPA-biPy) chelating ligands (**L1**-**L4**), Scheme 1. Additionally, TPA-biPy chelating ligands were synthesized by the classical Suzuki reaction (**L1**-**L3**) [33] and Wittig reaction (**L4**) [34]. The ultimate *trans*-configuration of **L4** was obtained by the reflux reaction using a catalytic amount of iodine, which was proved by the hydrogen nuclear magnetic resonance (^{1}H NMR) spectrum (hydrogen atoms of the double bonds are shown in 6.97 ppm with the coupling constant of 16.2 Hz [35]). Target complexes were isolated as PF_6 salts, obtained with favorable yield (61–74%). Multiple attempts to grow single crystals failed due to the "propeller" structure and the introduction of terminal flexible substituents (-OCH_3) for TPA units increasing the steric hindrance of target Ir^{III} complexes. Instead, they were characterized by infrared spectroscopy (IR), nuclear magnetic resonance (^{1}H and ^{13}C NMR) spectroscopy, mass spectrometry (MS) and elemental analysis (Figs. S1–S4). These complexes were soluble in common organic solvents such as dichloromethane, methanol and dimethyl sulfoxide, insoluble in the ether and hexane. Aqueous stability of complexes **1–4** was also determined in 50% CH_3OH/50% H_2O (v/v) by ultraviolet-visible (UV–vis) absorption spectrum at 298 K for 8 h, and no obvious changes were observed (Fig. S5). The studies confirm that TPA-appended cyclometallated Ir^{III} complexes possess sufficient stability for the application of biological assays.

2.1. Photophysical properties

Due to the advantage of short excited state lifetime, high thermostability and easily adjustable emission color, cyclometallated Ir^{III} complexes, the most popular luminous materials, have been extensively used in the field of organic photoelectric field. [36] Photophysical properties of complexes **1–4** were determined by UV–vis spectrum and photoluminescence (PL) spectra. As shown in Fig. 2 and Table 1, complexes **1–4** show almost the same photophysical properties, which have a strong intraligand absorption band (π-π*) at around 250–280 nm ($\varepsilon > 18{,}000\ M^{-1}\ cm^{-1}$) and a relatively weaker metal-to-ligand charge-transfer (MLCT) transition band at around 350–500 nm. The room-temperature PL spectra showed that complexes **1–4** exhibited an intense yellow emission located at ~600 nm. [37,38]

To further understand how the ancillary ligands (TPA-modified bipyridine) influence the photophysical properties of target complexes, the optimal configurations, the frontier molecular orbitals and their electron cloud distribution were analyzed by density functional theory (DFT) calculation at the B3LYP/6-31G(d) (C, H, N, Cl)/lanl2dz (Ir) level. [39] As shown in Fig. 3, the highest occupied molecular orbitals (HOMOs) of complexes **1–4** are mainly localized on the bipyridine ligand and the terminal TPA groups, while the lowest unoccupied molecular orbitals (LUMOs) are mainly localized on the central iridium atom, bipyridine ligand and phenyl of TPA molecule connected with bipyridine, which indicate that the introduction of TPA molecule improves the conjugate area of bipyridine chelating ligand [40], thus increasing conjugate power of the whole target complexes. The dihedral angles (θ) between **P2** and **P3** (benzene ring in TPA units, Table 1) are almost the same numerically, which confirmed that the introduction of terminal methoxyl has little effect on the TPA group. However, the dihedral angles between **P1** (pyridine ring) and **P2** (benzene ring of TPA molecule) are 24.80°, 28.92°, 25.80° and 3.55° for complexes **1–4**, respectively. Due to the introduction of *trans*-double bond, the minor dihedral angle of complex **4** increase the conjugate power of the whole

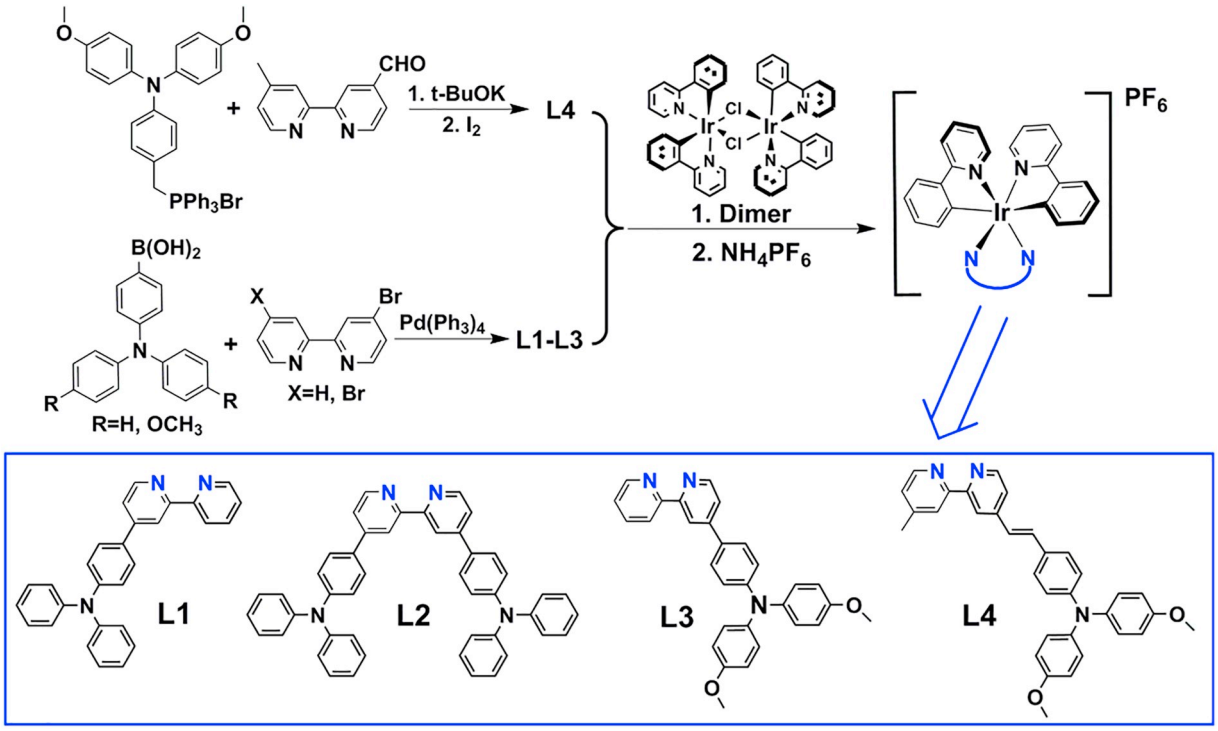

Scheme 1. Synthesis process of cyclometalated Ir^{III} complexes.

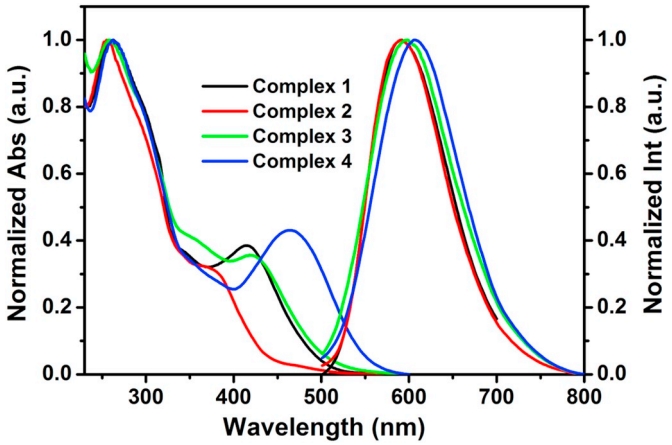

Fig. 2. Normalized UV–vis and PL of complexes **1–4** in methanol solution (1.0×10^{-5} mol L^{-1}).

Table 1
Optical and structural optimization parameters of target complexes.

Complex	λ_{ab}/nm (ε, 10^5 M^{-1} cm^{-1})[a]	λ_{em}/nm[b]	θ/°[c]	
			P1-P2	P2-P3
1	263 (2.42), 415 (0.94)	591	24.80	66.82
2	255 (2.39), 388 (0.65)	590	28.92	66.29
3	259 (1.88), 418 (0.68)	599	25.80	67.41
4	265 (2.31), 465 (1.01)	606	3.55	68.50

[a] The maximum absorption peak of UV–vis was recorded in the 1.0×10^{-5} mol L^{-1} methanol solution.
[b] PL spectra were recorded with excitation wavelength at maximum absorption peak.
[c] The dihedral angles (θ) of optimized structure.

complexes, and endowed with the bigger UV–vis and PL wavelength compared with other complexes, and which further confirmed why complexes **1–3** show almost the same photophysical properties.

2.2. Cytotoxicity test

The cytotoxicity of target Ir^{III} complexes was evaluated by the standard MTT (3-(4,5-dimethylthiazol-2-yl)-2,5- diphenyltetrazolium bromide) assay towards A549 (lung cancer cell, the leading cause of death in both developed and developing countries [41]) cells as a model cancer cell line in vitro. The IC_{50} values (50% inhibitory concentration) of target Ir^{III} complexes, TPA-unattached structural Ir^{III} complexes [Ir $(ppy)_2(biPy)]PF_6$ (complex **5**, Scheme S2), *cis*-platin and dimer of iridium are listed in Table 2. As shown, except for complex **2**, the other three complexes show better antineoplastic activity towards A549 cells than the dimer, *cis*-platin and complex **5**, the best of which (complex **1**) was nearly five times of *cis*-platin and ten times of TPA-unattached structural complex **5**. Due to the minor difference in structure, complexes **1**, **2** and **4** show almost the similar antineoplastic activity. However, for complex **2**, the more TPA substituents, the less active it is. Our previous studies have verified that the antineoplastic activity of Ir^{III} complexes can be effectively improved by the adjustment of lipid and water solubility of complexes [42,43]. The partition coefficients (*logP*) of complexes **1–4** in oil/water was determined by inductively coupled plasma mass spectrometry (ICP-MS), and the values were −0.13, 0.98, −0.18 and −0.23, respectively. These results indicate that the introduction of too many TPA groups enhances the lipid solubility of complex **2**, but at the same time weakens its water solubility, thus affecting the antineoplastic activity of these complexes.

In addition, the cytotoxicities of complexes **1–4** to human bronchial epithelial cells (16HBE) and lung epithelial cells (BEAS-2B) were further evaluated. As shown in Table 2, complexes **1–3** show almost no selectivity for cancer cells versus normal cells, however, complex **4** show some selectivity. This conclusion indicates the introduction of double bond is beneficial to enhance the selectivity of this kind of complex, which provides a structural basis for the later optimization of structure in future work.

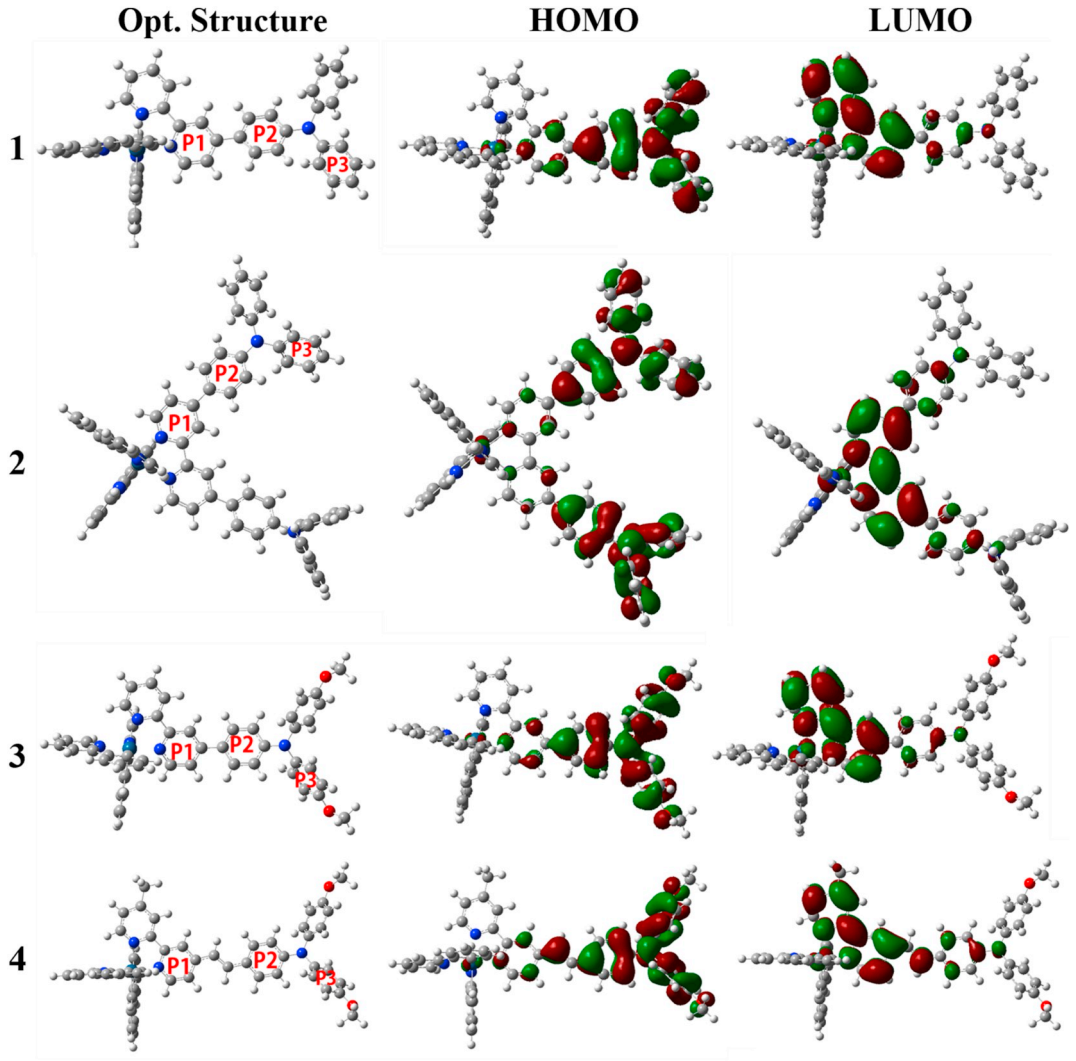

Fig. 3. Calculated optimal configurations, HOMO and LUMO diagrams of complexes **1**–**4**.

Table 2
IC_{50} values of Ir^{III} complexes, *cis*-platin and dimer towards A549, BEAS-2B and 16HBE cells after 24 h.

Complex	IC_{50} (μM)		
	A549	BEAS-2B	16HBE
$[Ir(ppy)_2(\mathbf{L1})]PF_6$ (**1**)	4.34 ± 0.01	5.48 ± 1.21	5.99 ± 0.81
$[Ir(ppy)_2(\mathbf{L2})]PF_6$ (**2**)	80.91 ± 8.65	> 100	83.87 ± 4.23
$[Ir(ppy)_2(\mathbf{L3})]PF_6$ (**3**)	5.80 ± 0.21	5.80 ± 0.61	2.56 ± 0.36
$[Ir(ppy)_2(\mathbf{L4})]PF_6$ (**4**)	10.80 ± 0.11	> 100	> 100
$[Ir(ppy)_2(biPy)]PF_6$ (**5**)	40.33 ± 0.82	/	/
cis-platin	21.30 ± 1.71	/	/
Dimer	57.70 ± 0.81	/	/

2.3. Metastasis inhibition

Metastasis is really troublesome problem in the later period of cancer evolution. Malignant tumor cells possess the capacity, migrate to non-malignant tissue of distant and survive there. [44,45] Therefore, metastasis inhibition plays a crucial role in advanced cancer treatment. The effects of complex **1** and **4** on antimetastasis for A549 cells were evaluated by wound healing migration assays. As shown in Fig. 4, obvious migration of A549 cells and wound closure were found in control (no drugs) after 24 h. However, for complexes **1** and **4**, extensive wound remained uncovered with the concentration of 0.25 × IC_{50}. Compared with complex **4**, the effect of **2** is more distinct. The wound closure ratio was 7.5% and 18.8% for complexes **1** and **4**, respectively, which was consistent with the result of the MTT assay (complex **1** show better anticancer activity than **4**). The results confirm that target Ir^{III} complexes possess the potential effect on the metastasis of cancer cells, which are helpful for cancer therapy.

2.4. Reaction with BSA

As a transport protein in vivo, serum albumin (SA) provides a "carrier" for drugs to reach the lesion. Studying the binding properties between antitumor drugs and SA is crucial to understand the mechanism of action. [46] Due to the favorable binding features and similar to human serum albumin (HSA) structure, bovine serum albumin (BSA) could be an inexpensive model for studying the transport mechanism of drugs in organisms. [47] Therefore, in this study, BSA was used to identify the reaction progress of target complexes with transport protein.

As shown in Figs. 5a and S6, with the increase of cyclometallated Ir^{III} TPA complexes, the maximum absorption of 218 nm (the absorption of BSA) decreased, which indicated that these complexes could affect BSA and lead to alpha helical interference. Additionally, a

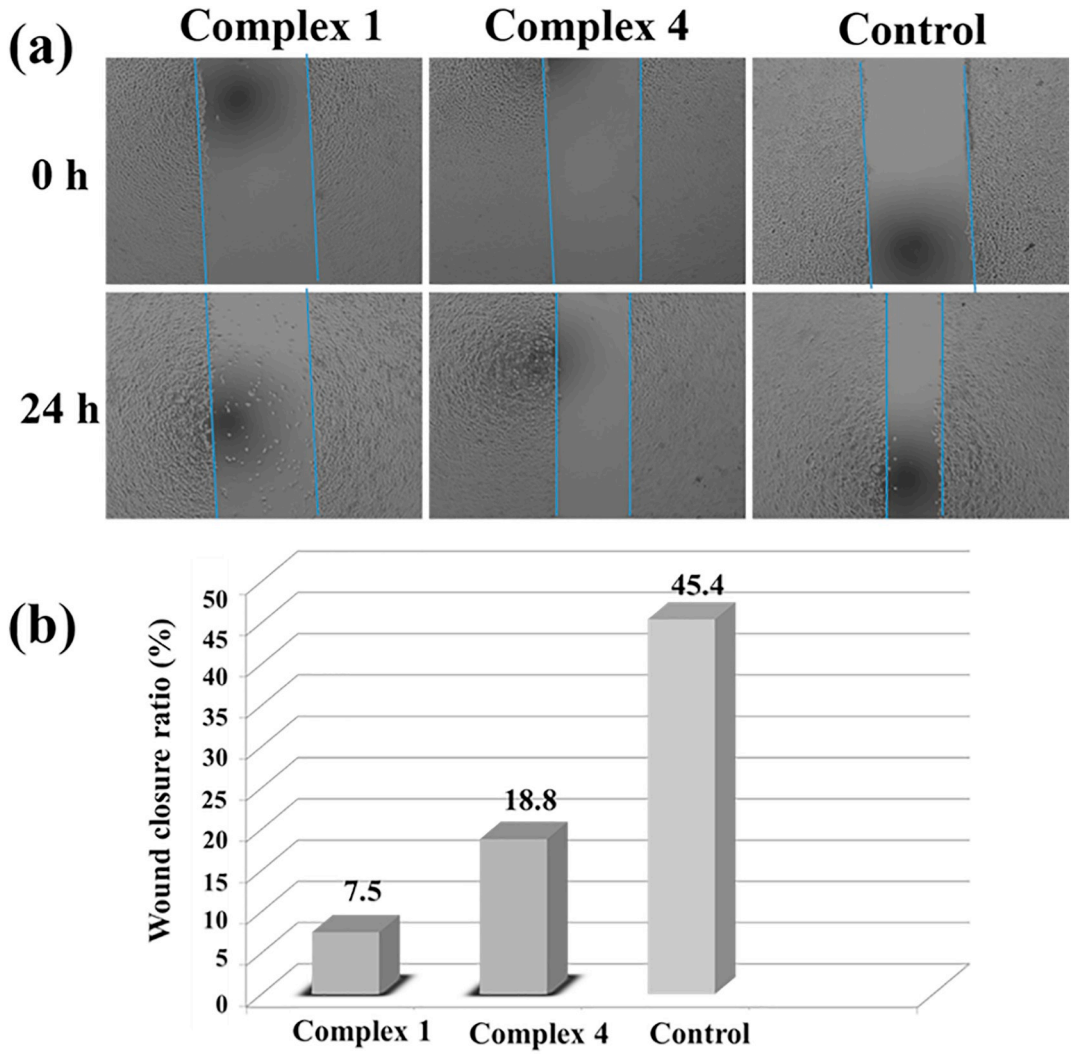

Fig. 4. Wound healing assay of A549 cells treated with or without complexes (**1** and **4**) for 24 h. (a) Images were obtained after 0 and 24 h. (b) Histograms of wound healing assay after 24 h. Data are quoted as mean ± SD of three replicates.

significant red shift was found at 218 nm due to the influence of polar solvent (water) [48]. Meanwhile, the absorption intensity at 278 nm increase along with the addition of complexes, which is related to the presence of aromatic acid residues (tryptophan, tyrosine and phenylalanine) in BSA [49]. Simultaneous fluorescence spectra were used to determine the detailed changes of microenvironment around BSA under

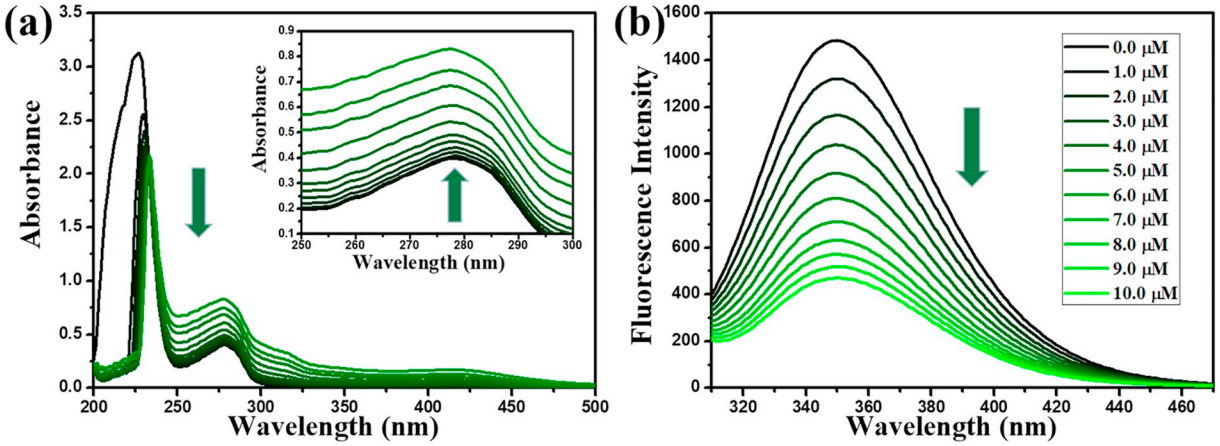

Fig. 5. (a) Absorbance of BSA (10 μM) was determined by UV–vis spectra after incubated with complex **1** (0–10 μM) in Tris-HCl/NaCl buffer solution (pH = 7.2) at 298 K. Inset: Changes of wavelength from 250 to 300 nm. (b) The fluorescence intensity of BSA (10 μM) obtained after reacted with complex **1** (0–10 μM) in Tris-HCl/NaCl buffer solution (pH = 7.2) at 298 K. The arrows showed the changes with the increase of complex.

Table 3
The values of K_{sv}, K_b, K_q and n for complexes **1**–**4** at 298 K.

Complexes	K_{sv} (10^5 M^{-1})	K_q (10^{13} M^{-1} S^{-1})	K_b (10^4 M^{-1})	n
1	1.23 ± 0.14	1.23	14.57	1.02
2	2.29 ± 0.13	2.87	10.19	0.96
3	1.64 ± 0.10	1.64	12.13	0.96
4	0.94 ± 0.17	0.94	10.67	0.91

the similar conditions, particularly near the fluorophore [50]. In this study, tyrosine and tryptophan, aromatic acid residues of BSA, were detected through the wavelength interval of $\Delta\lambda$ = 15 nm and 60 nm by a synchronous fluorescence. The weakened of fluorescence intensity at 291 nm and 285 nm ($\Delta\lambda$ = 15 nm and 60 nm, respectively) for complexes **1**–**4** were shown in Figs. S8 and S9. Interestingly, there is a minor shift (2–3 nm) at $\Delta\lambda$ = 15 nm, however, almost no change occurs at the wavelength of $\Delta\lambda$ = 60 nm, which indicate that tyrosine residues of BSA is more involved in the interaction with target complexes, other than tryptophan [51].

Fluorescence emission spectra were further employed to detect the binding characteristics between cyclometallated Ir^{III} TPA complexes and BSA. As shown in Figs. 5b and S7, with the increase of complexes, the fluorescence intensity of BSA rapidly quenched. The Stern-Volmer quenching constant K_{sv}, the quenching rate constant K_q, the binding constant K_b and the number of binding sites n were determined by classical Stern-Volmer equation [52] (Fig. S10) and the Scatchard equation [53] (Fig. S11). As shown in Table 3, the K_q values of cyclometallated Ir^{III} TPA complexes are nearly three orders of magnitude (10^{13} M^{-1} s^{-1}) higher than that of the pure dynamic quenching mechanism, which is sufficient to demonstrate that cyclometallated Ir^{III} TPA complexes binding to BSA primarily follows the static quenching mechanism [54]. In spite of almost the same number of binding sites (n), complex **1** show the larger binding constant (K_b) than the other three complexes, which is consistent with the result of cytotoxicity test.

2.5. Apoptosis assay

Cell function decline was often associated with apoptosis. In this study, flow cytometry was used to determine that by means of A549 cells treated with target complexes after stained with Annexin V-FITC/PI. [55] As shown in Fig. 6 and Tables S1-S2, after incubated with complexes **1** and **4** (0.5 × IC_{50}, 1.0 × IC_{50}, 2.0 × IC_{50} and 3.0 × IC_{50}) for 24 h, the values of the late apoptotic phase indicate a significant increase in a dose-dependent manner. With the concentration of incubation changed from 0.5 × IC_{50} to 3.0 × IC_{50}, the proportion of late apoptosis increase by 67.3% and 63.8% for complexes **1** and **4**, respectively. However, above 86% cells survive for the control under the same conditions. This result further confirmed that cyclometallated Ir^{III} TPA complexes could induce cell function decline and lead to apoptosis.

2.6. Cell cycle analysis

To investigate whether apoptosis is the result of cell cycle arrest induced by cyclometallated Ir^{III} complexes, flow cytometry was used to measure the changes of cell cycle of A549 cells after treated by complexes **1** and **4** with the concentration of 0.25 × IC_{50}, 0.5 × IC_{50}, 1.0 × IC_{50} and 2.0 × IC_{50} for 24 h. As shown in Fig. 7 and Tables S3–S4, **1** and **4** mainly lead to cell arrest in G_0/G_1 phase with the population of 66.0% and 56.6%, respectively. Compared with control, which nearly increased by 8.5% and 8.6%. This conclusion indicates that cyclometallated Ir^{III} TPA complexes might restrain the proliferation of A549 cells to some extent by cell cycle arrest, and eventually leading to apoptosis.

2.7. Mitochondrial membrane potential (MMP)

Mitochondria, the main energy producing sites of cells, play the vital role in apoptosis. Once the integrity of mitochondrial membrane is destroyed, which might release signal and lead to mitochondrial dysfunction, and then induce apoptosis. The degree of mitochondrial dysfunction could be evaluated by measuring the changes of mitochondrial membrane potential (MMP). [56] A549 cells were incubated with complexes **1** and **4** for 24 h at the concentrations of 0.25 × IC_{50}, 0.5 × IC_{50}, 1.0 × IC_{50} and 2.0 × IC_{50}, and stained by JC-1 (a commonly used fluorescent probe to evaluate MMP). JC-1 monomer (green)/JC-1 aggregate (red) as shown in Fig. 8 and Tables S5-S6. Compared with negative control, a significant concentration-dependent increase was demonstrated at the indicated concentrations. The population of mitochondrial membrane depolarized cells increased by 24.4% and 28.1% for complexes **1** and **4** with the concentration changed from 0.25 × IC_{50} to 2.0 × IC_{50}, respectively. This observation suggests that cyclometallated Ir^{III} TPA complexes can cause cancer cell death through the dysfunction of MMP.

2.8. Cell uptake and cellular localization

Cell imaging is a key crucial criteria to evaluate targeting sites of complex, especially for real-time. Due to favorable luminescence property of cyclometallated Ir^{III} TPA complexes, laser confocal microscopy was used to determine the intercellular colocalization of A549 cells. [8] Additionally, Lyso Tracker Red DND-99 (LTRD) and Mito Tracker Deep Red (MTDR) were utilized as lysosomes and mitochondria fluorescence probes. As shown in Fig. 9, complexes **1** and **4** could effectively accumulate in lysosomes with the Pearson's co-localization coefficient (PCC) of 0.97 and 0.98 after incubated for 6 h. However, the PCC of mitochondrion-targeted is 0.12 and 0.13 for complexes **1** and **4**, respectively. The results indicate that the introduction of TPA group containing nitrogen atoms with free electron pairs facilitates the targeting of acidic lysosomes in vivo for these Ir^{III} TPA complexes. [16–21] Interestingly, target complexes did not cause abnormal cell death immediately, which made it easy to track changes in lysosomal morphology timely.

Due to the accumulation in lysosome for cyclometallated Ir^{III} TPA complexes, lysosomal damage assays were performed towards complex-treated A549 cells to gain insight into the effects on lysosomes and their surroundings. In this study, acridine orange (AO), an effective probe for red fluorescence in lysosomes and green fluorescence in cytoplasm and nucleus, was used to evaluate the lysosomal integrity. As shown in Fig. 10, compared with control, there was a significant decrease in red fluorescence and increase in green fluorescence when hatched in complexes **1** and **4** (10 μM) for 1 h, and obvious lysosomal damage was found after 6 h. The results confirmed that cyclometallated Ir^{III} TPA complexes could target lysosome, lead to lysosomal damage and the release of cathepsins and other hydrolases from the lysosomal lumen to the cytosol, and eventually induce apoptosis. [13] Meanwhile, this conclusion also explains why cyclometallated Ir^{III} TPA complexes do not target mitochondria, but MMP changes significantly, which is mainly due to the lysosomal damage.

Cellular uptake mechanisms of drugs fall into two broad categories: energy demand mechanism (divided into active transport and endocytosis) and non-energy demand mechanism (divided into passive transport and free diffusion) [57]. In this study, chloroquine (endocytosis inhibitors) and carbonyl cyanide *m*-chlorophenylhydrazine (CCCP, energy inhibitors) were used to determine the cellular uptake mechanisms of cyclometallated Ir^{III} TPA complexes. A549 cells were incubated with complexes **1** and **4** at 277 K and 310 K for 2 h, and then treated with chloroquine and CCCP. As shown in Figs. S12 and S13, there were almost no changes compared with control, which confirmed that the way of target complexes enter A549 cells is independent of endocytosis and energy, therefore, corresponding to the mechanisms of

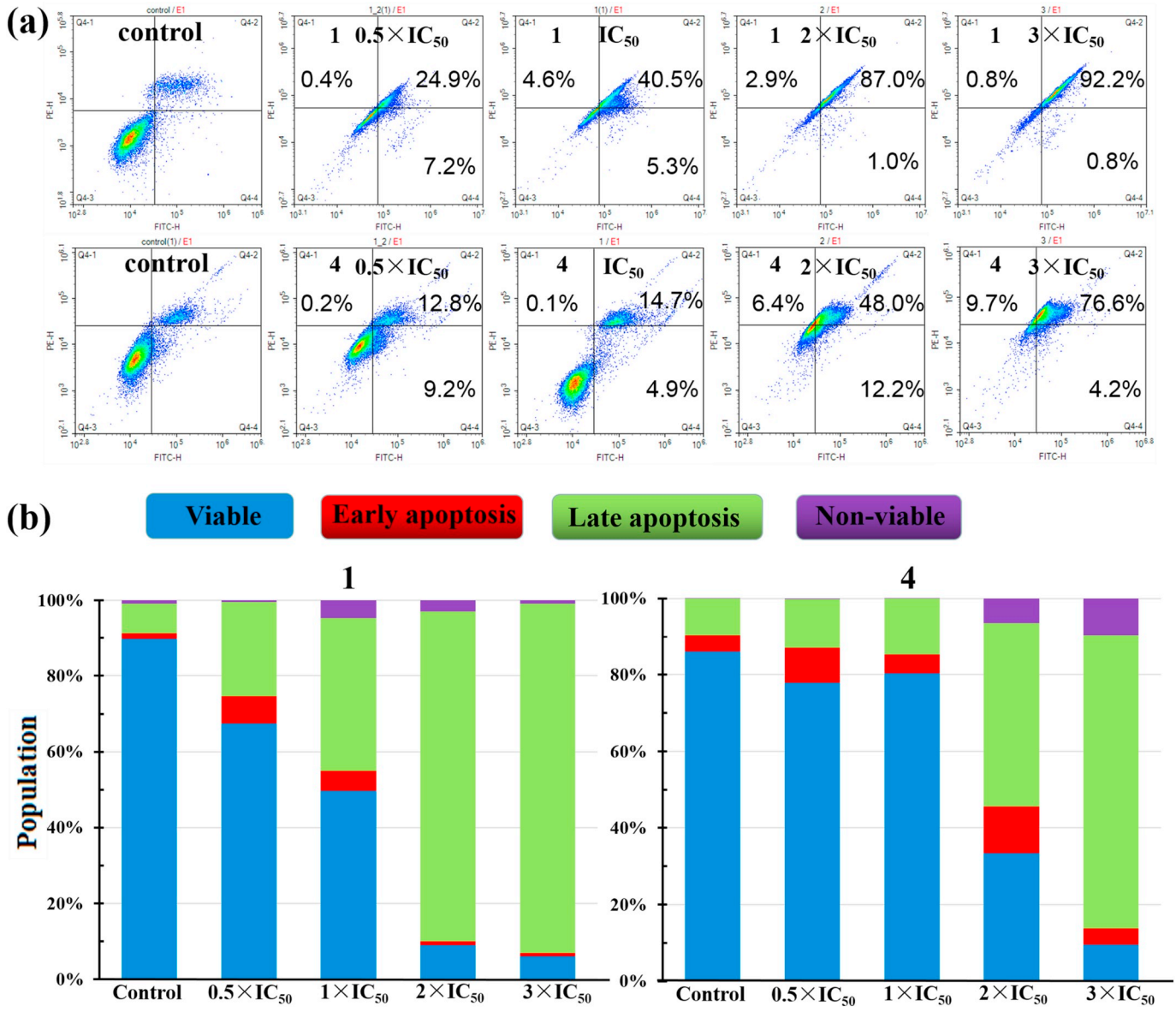

Fig. 6. (a) Apoptosis of A549 cells was analyzed by flow cytometry after incubated with selected complexes **1** and **4** (concentrations: 0.5, 1.0, 2.0, 3.0 × IC_{50}) and stained by Annexin V-FITC/PI for 24 h at 310 K. (b) Histograms of four stages induced by complexes **1** and **4**. Data was averaged for three replicate experiments ± SD.

non-energy dependent cell uptake.

2.9. Antibacterial and bactericidal activity

In this study, the minimum inhibitory concentration (MIC) of cyclometallated Ir^{III} TPA complexes against *Escherichia coli* (*E. coli*, ATCC 8739) at 37 °C was determined by microcalorimetry. [58] As shown in Figs. 11a and S14, the thermal power-time curves, which indicate the growth rate of *E. coli*, were processed at different concentrations by classical Logistic equation (Eq. (1)).

$$P_t = P_m/(1 + \alpha e^{-\mu t}) \quad (1)$$

where μ is the growth rate constant, α is the integral constant, P_m and P_t are the maximum heat production rate and the heat production rate at time t, respectively. The measured experimental data P_m, P_t and t were analyzed in the measured power-time curve. The growth rate constant μ was obtained by linear regression analysis and further established the relationship with the inhibitory concentration (C). As shown in Figs. 11b and S15, the minimum inhibitory concentration was obtained when $\mu = 0$. Antibacterial data were presented in Table 4, cyclometallated Ir^{III} TPA complexes show certain antibacterial activity against *E. coli*. However, compared with Penicillin sodium (common antibacterial on the market), there is still a big gap (almost ten times) for target complexes. Which indicate that the potential applications of cyclometallated Ir^{III} TPA complexes in the antibacterial field are limited.

3. Conclusions

Four TPA-appended cyclometallated Ir^{III} complexes were synthesized and characterized. Target complexes had a certain inhibitory effect on *E. coli*. More importantly, complexes showed potential anticancer activity against A549 cells, the best of which (complex **1**) was nearly five times of *cis*-platin and ten times of TPA-unattached structural Ir^{III} complexes, meanwhile, which could prevent the metastasis of cancer cells. Interestingly, complexe **4** show some selectivity for cancer cells versus normal cells. Complexes could transport trough serum protein and followed by a binding mechanism of static quenching

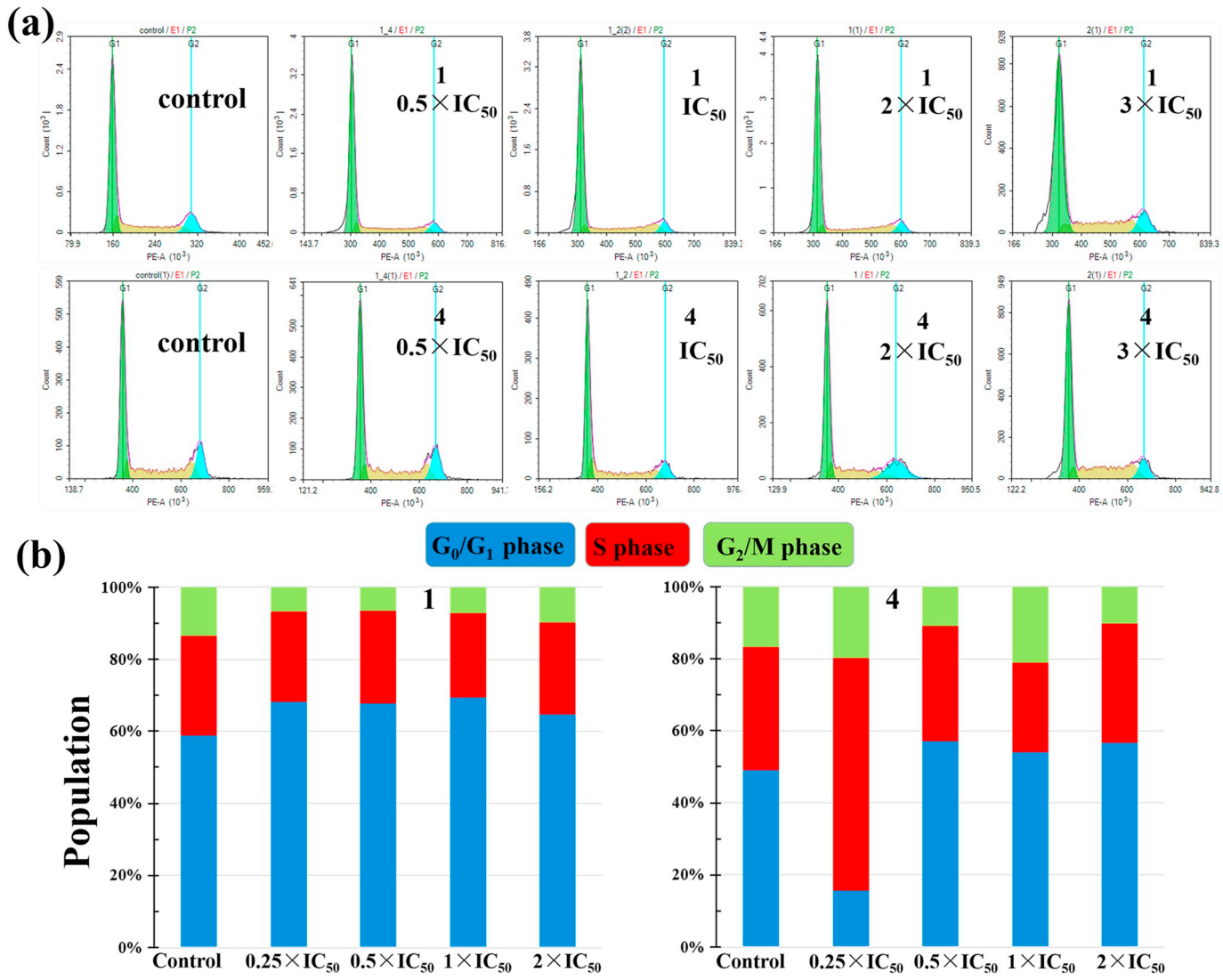

Fig. 7. (a) The altered A549 cell cycle was analyzed by flow cytometry after induced by complexes **1** and **4** (concentrations = 0.25, 0.5,1.0 and 2.0 × IC_{50}) for 24 h at 310 K. (b) Histograms of cell cycle distributions for complexes **1** and **4**. Data are quoted as mean ± SD of three replicates.

mode. Because of the favorable fluorescent properties of target Ir^{III} complexes, laser confocal microscopy confirmed the way enter cells is corresponding to the mechanism of non-energy dependent, accumulate in lysosome and lead to lysosomal damage, which induce the release of lysozyme, thereby affecting mitochondrial membrane potential, disrupt the cell cycle and induce apoptosis. Above all, TPA-appended cyclometallated Ir^{III} bipyridine complexes are potential anticancer agents with dual functions, including metastasis inhibition and lysosomal damage.

4. Experimental section

4.1. General information

Iridium trichloride, iodine, 2-phenylpyridine, 4,4′-dimethyl-2,2′-bipyridyl, selenium dioxide, anhydrous potassium carbonate, *n*-butyllithium, 4,4′-dibromo-2,2′-bipyridine, 4-bromo-2,2′-bipyridine, 4-bromotriphenylamine, 4-formyltriphenylamine, sodium borohydride, triphenyl phosphine hydrobromide, triisopropyl borate, tetratriphenylphosphine palladium, potassium tert-butanolate and all kinds of organic solvents (methanol, tetrahydrofuran, methylbenzene etc.) were purchased from Rhea biotechnology co. LTD. DMEM medium, fetal bovine serum, penicillin/streptomycin mixture, trypsin/EDTA, and phosphate-buffered saline (PBS) were purchased from Sangon Biotech. A549 lung cancer cells and human bronchial epithelial normal cells (16HBE and BEAS-2B) were obtained from Shanghai Institute of Biochemistry and Cell Biology (SIBCB). Dimer of iridium ($[Ir(ppy)_2Cl]_2$) [59] and chelating ligands (**L1**-**L4**) were synthesized according to the methods of literatures [33,34,42] (Scheme S1), the data were shown in supporting information.

NMR spectra were obtained on Bruker DPX 500 spectrometers instrument, with the chemical shifts reported in ppm using tetramethylsilane (TMS) as an internal standard. Mass spectrum (ESI-MS) was measured on a LCQ Advantage MAX mass spectrometer. Elemental analysis was performed on a VarioMICRO CHNOS elemental analyzer. IR spectra were recorded on a Nicolet Nexus 470 FT-IR spectrophotometer using KBr discs in the range 4000–400 cm^{-1}. UV–vis spectroscopy was performed on a PERSEE TU-1901 UV spectrometer. Fluorescence spectra were collected by a Hitachi F-4600 fluorescence spectrophotometer, with a 400 V voltage and 5 nm slit width for both excitation and emission. Induction of apoptosis, cell cycle and mitochondrial membrane potential (MMP) determination were carried out by an ACEA Novocyte2040R flow cytometry. Viability assay (MTT) was measured using a Perlong DNM-9606 microplate reader at an

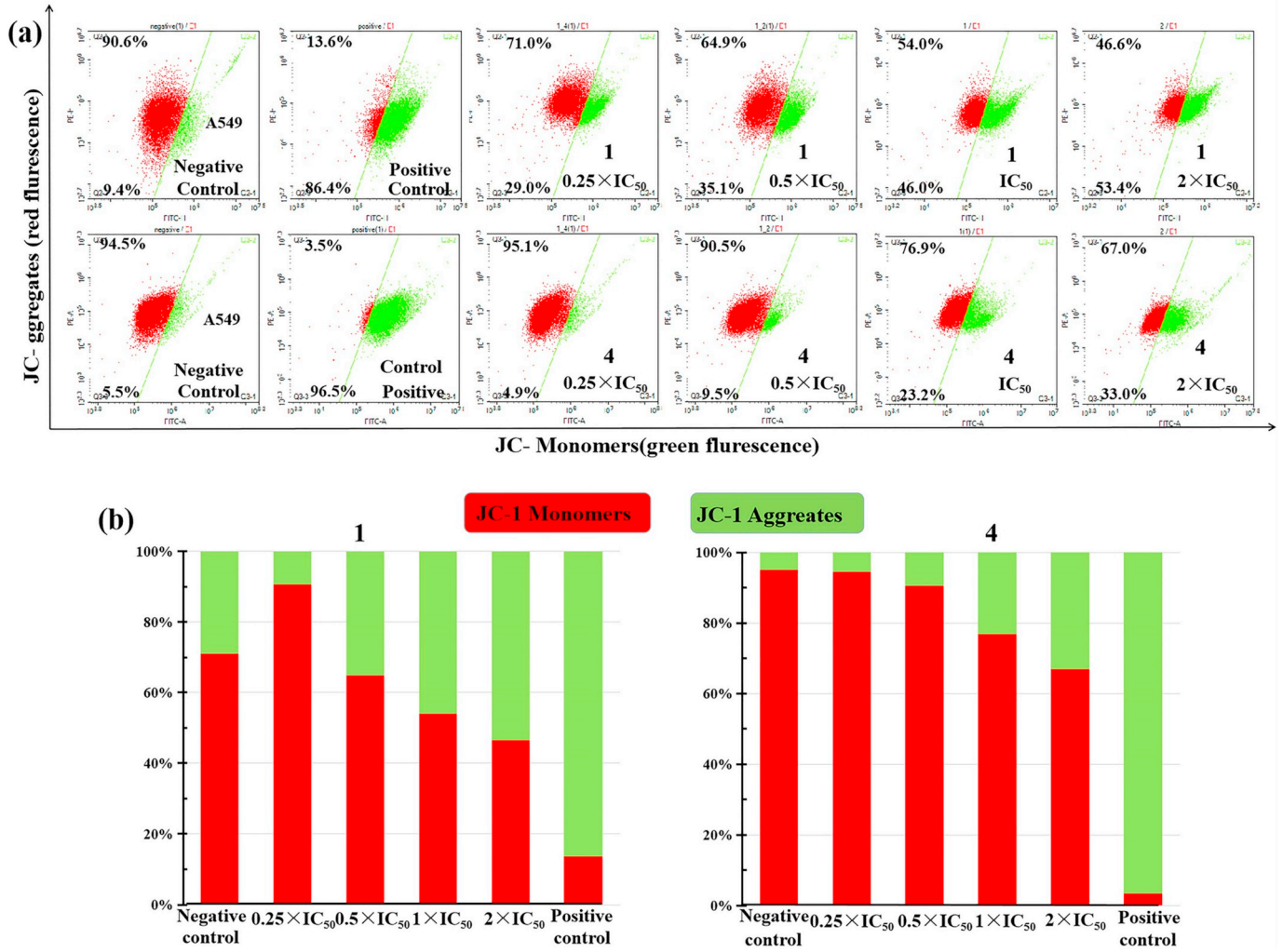

Fig. 8. (a) Changes of JC-1 monomer (green)/JC-1 aggregate (red) induced by complexes **1** and **4** (concentrations = 0.25, 0.5, 1.0 and 2.0 × IC_{50}). (b) Histograms for the JC-1 monomers/JC-1 aggregates treated with complexes **1** and **4**. Data are quoted as mean ± SD of three replicates.

absorbance of 570 nm. Cell uptake and cellular localization were carried out on a Carl Zeiss AG */LSM/880NLO two photon laser Scanning microscope. Antibacterial activity was measured by Thermometric AB 3114/3236 Thermal Activity Monitor (TAM) Air Isothermal Calorimeter.

4.2. Synthesis of target complexes (1–4)

General procedure: $[Ir(ppy)_2Cl]_2$ (Dimer, 53.6 mg, 0.05 mmol) and chelating ligands (**L1**-**L4**, 0.10 mmol) were mixed in methanol (80 mL) under nitrogen atmosphere. After stirred 12 h at room temperature, 65.2 mg (0.40 mmol) ammonium hexafluorophosphate were added to above solution and reacted for another 6 h. The solvent was removed by a rotary evaporator and the crude product recrystallized from methanol and ether. Purification product was rinsed with *n*-hexane and dried in vacuo. The IR (KBr), ^{1}H NMR (500 MHz), ^{13}C NMR (126 MHz), ESI-MS and element analysis of complexes **1–4** are shown in Figs. S1–S4. The data were listed as follows:

$[Ir(ppy)_2$(**L1**)$]PF_6$ (**1**). Yield: 67.0%. Selected IR (KBr): 1604.0, 1588.3, 1501.4, 1329.9, 762.2 cm^{-1}; ^{1}H NMR (500 MHz, DMSO) δ 9.13 (d, J = 8.2 Hz, 1H), 9.06 (s, 1H), 8.28 (dd, J = 13.9, 7.2 Hz, 3H), 7.98–7.91 (m, 6H), 7.89 (d, J = 5.5 Hz, 1H), 7.77 (d, J = 5.9 Hz, 1H), 7.73–7.68 (m, 2H), 7.65 (d, J = 5.7 Hz, 1H), 7.39 (t, J = 7.9 Hz, 4H), 7.27–7.22 (m, 1H), 7.22–7.10 (m, 8H), 7.06–6.99 (m, 4H), 6.91 (t, J = 7.4 Hz, 2H), 6.21 (d, J = 7.6 Hz, 2H). ^{13}C NMR (126 MHz, DMSO) δ 167.37, 167.33, 156.24, 156.08, 151.41, 151.08, 150.26, 150.18, 150.07, 149.87, 149.36, 146.66, 144.34, 144.30, 140.00, 139.22, 131.58, 130.72, 130.33, 129.31, 127.66, 125.82, 125.57, 124.99, 124.44, 122.71, 121.65, 121.29, 120.55. ESI-MS (m/z): $[M\text{-}Cl]^+$ Calcd for $C_{50}H_{37}IrN_5$, 900.1; Found 900.5. Elemental analysis: Found: C, 57.81; H, 3.61; N, 6.61%, calcd for $C_{50}H_{37}N_5PF_6Ir$: C, 57.56; H, 3.64; N, 6.63%%.

$[Ir(ppy)_2$(**L2**)$]PF_6$ (**2**). Yield: 73.3%. Selected IR (KBr): 1607.3, 1586.4, 1498.6, 1334.1, 1279.9, 757.7, 699.7 cm^{-1}; ^{1}H NMR (500 MHz, DMSO) δ 9.23 (s, 2H), 8.29 (d, J = 8.2 Hz, 2H), 7.96 (dd, J = 14.0, 8.0 Hz, 10H), 7.82 (d, J = 5.9 Hz, 2H), 7.74 (d, J = 5.7 Hz, 2H), 7.39 (t, J = 7.9 Hz, 8H), 7.23–7.15 (m, 6H), 7.14–7.10 (m, 8H), 7.03 (t, J = 7.5 Hz, 6H), 6.92 (t, J = 7.4 Hz, 2H), 6.24 (d, J = 7.4 Hz, 2H). ^{13}C NMR (126 MHz, DMSO) δ 167.40, 156.37, 151.56, 150.07, 150.00, 149.37, 146.67, 144.36, 139.21, 131.59, 130.72, 130.32, 129.47, 127.92, 125.75, 125.59, 125.29, 125.10, 124.95, 124.46, 122.67, 121.88, 121.37, 120.54. ESI-MS (m/z): $[M\text{-}Cl]^+$ Calcd for $C_{68}H_{50}IrN_6$, 1143.4; Found 1143.8. Elemental analysis: Found: C, 63.69; H, 3.92; N, 6.47%, calcd for $C_{68}H_{50}N_6PF_6Ir$: C, 63.45; H, 3.96; N, 6.44%.

$[Ir(ppy)_2$(**L3**)$]PF_6$ (**3**). Yield: 68.2%. Selected IR (KBr): 1607.0, 1561.8, 1503.7, 1329.1, 1251.2, 845.1, 762.2 cm^{-1}; ^{1}H NMR (500 MHz, DMSO) δ 9.11 (d, J = 8.4 Hz, 1H), 9.00 (s, 1H), 8.31–8.24 (m, 3H), 7.97–7.90 (m, 5H), 7.87 (dd, J = 11.7, 7.1 Hz, 3H), 7.73 (d, J = 6.0 Hz, 1H), 7.69 (t, J = 6.0 Hz, 2H), 7.64 (d, J = 5.1 Hz, 1H),

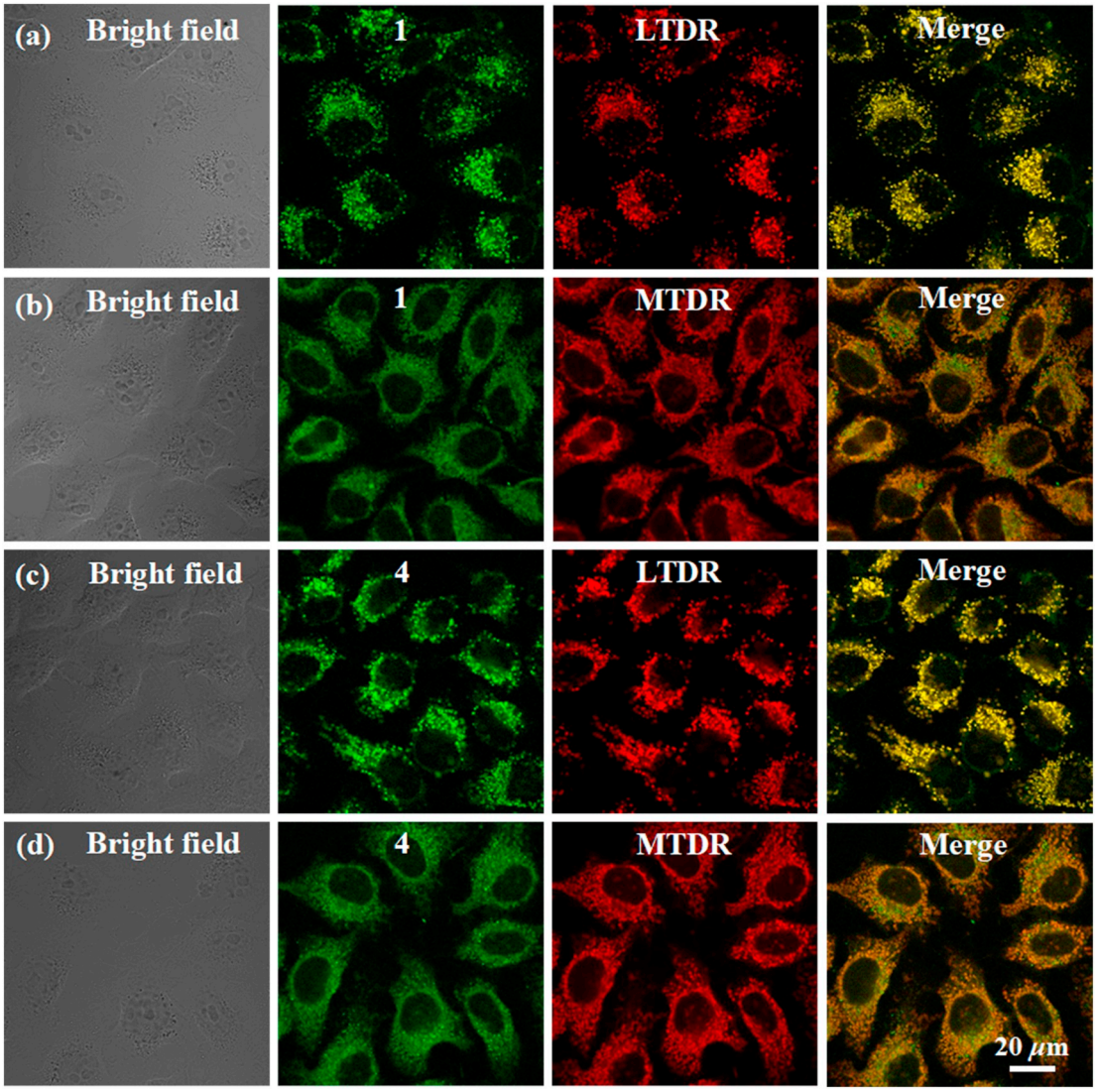

Fig. 9. Intercellular colocalization of complexes **1** (a, b) and **4** (c, d) (15 μM, 1 h) with LTRD (100 nM, 30 min) and MTDR (50 nM, 30 min) in A549 cells. Scale bars: 20 μm.

7.17 (t, J = 6.6 Hz, 2H), 7.13 (d, J = 8.9 Hz, 4H), 7.02 (t, J = 7.6 Hz, 2H), 6.98 (d, J = 9.0 Hz, 4H), 6.91 (t, J = 7.4 Hz, 2H), 6.81 (d, J = 9.0 Hz, 2H), 6.21 (dd, J = 7.2, 4.1 Hz, 2H), 3.76 (s, 6H). ^{13}C NMR (126 MHz, DMSO) δ 167.39, 167.33, 157.13, 156.11, 151.49, 151.23, 151.14, 150.26, 150.03, 149.95149.35, 144.36, 144.29, 140.59, 139.96, 139.28, 131.57, 130.71, 129.10, 128.20, 125.72, 125.55, 125.32, 124.42, 122.69, 121.17, 120.52, 117.89, 115.65, 55.78. ESI-MS (m/z): [M-Cl]$^+$ Calcd for $C_{52}H_{41}IrN_5O_2$, 960.1; Found 960.9. Elemental analysis: Found: C, 56.95; H, 3.75; N, 6.33%, calcd for $C_{52}H_{41}O_2N_5PF_6Ir$: C, 56.61; H, 3.80; N, 6.30%.

[Ir(ppy)$_2$(**L4**)]PF_6 (**4**). Yield: 61.3%. Selected IR (KBr): 1608.7, 1584.7, 1504.1, 1255.0, 845.6, 757.7 cm^{-1}; ^{1}H NMR (500 MHz, $CDCl_3$) δ 8.65 (d, J = 6.8 Hz, 2H), 7.90 (d, J = 8.5 Hz, 2H), 7.76 (d, J = 7.1 Hz, 2H), 7.72 (d, J = 6.0 Hz, 2H), 7.69 (dd, J = 9.3, 6.8 Hz, 3H), 7.59 (d, J = 5.6 Hz, 1H), 7.54 (d, J = 6.0 Hz, 1H), 7.50 (s, 1H), 7.47 (d, J = 2.4 Hz, 1H), 7.45 (s, 1H), 7.31 (d, J = 7.4 Hz, 1H), 7.16 (d, J = 5.7 Hz, 1H), 7.08 (d, J = 8.9 Hz, 3H), 7.06–7.00 (m, 5H), 6.93–6.89 (m, 3H), 6.86 (t, J = 9.0 Hz, 5H), 6.31 (d, J = 7.8 Hz, 2H), 3.81 (s, 6H), 2.64 (s, 3H). ^{13}C NMR (126 MHz, DMSO) δ 167.36, 156.92, 155.93, 155.72, 151.90, 151.56, 151.32, 150.29, 149.86, 149.34, 149.22, 148.70, 144.34, 139.59, 139.13, 137.42, 131.59, 130.66, 129.62, 129.27, 128.05, 127.03, 126.11, 125.52, 125.35, 124.39, 122.61, 121.04, 120.48, 118.22, 115.60, 55.76, 21.44. ESI-MS (m/z): [M-Cl]$^+$ Calcd for $C_{55}H_{45}IrN_5O_2$, 1000.2; Found 999.9. Elemental analysis: Found: C, 56.73; H, 3.85; N, 6.16%, calcd for $C_{54}H_{43}O_2N_5PF_6Ir$: C, 56.40; H, 3.90; N, 6.12%.

Abbreviations

ppy	phenylpyridine
biPy	bipyridine
TPA	Triphenylamine
TPA-biPy	Triphenylamine-modified bipyridine
SA	Serum Albumin
HSA	Human Serum Albumin
BSA	Bovine Serum Albumin
NADH	Reduced Form of Nicotinamide Adenine Dinucleotide
ICP-MS	Inductively Coupled Plasma Mass Spectrometry
log P	Partition Coefficient in Oil/Water
MTT	(4,5-Dimethylthiazol-2-yl)-2,5-diphenyltetrazolium bromide
ROS	Reactive Oxygen Species
MMP	Mitochondrial Membrane Potential
PCC	Pearson's Colocalization Coefficient
MIC	Minimum Inhibitory Concentration
E. coli	*Escherichia coli*

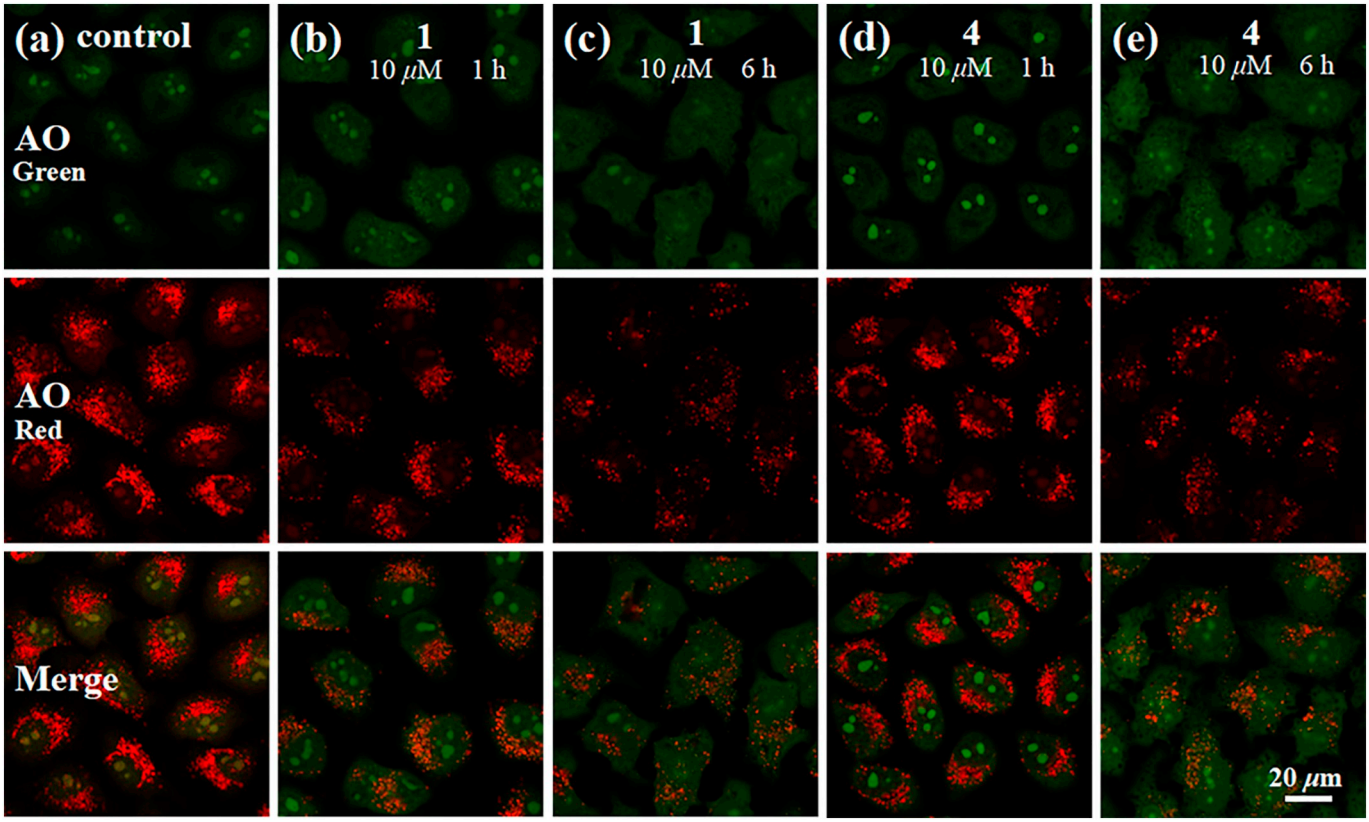

Fig. 10. Laser confocal images of A549 cells hatched by complexes **1** and **4**. (a) Control group; A549 cells were incubated in complex **1** (10 μM) for 1 h (b) and 6 h (c); A549 cells were in complex **4** (10 μM) for 1 h (d) and 6 h (**e**); All groups were stained with AO (5 μM) after incubation. λ_{ex} = 488 nm, λ_{em} = 510 ± 30 nm (green) and 625 ± 30 nm (red). Scale bar: 20 μm.

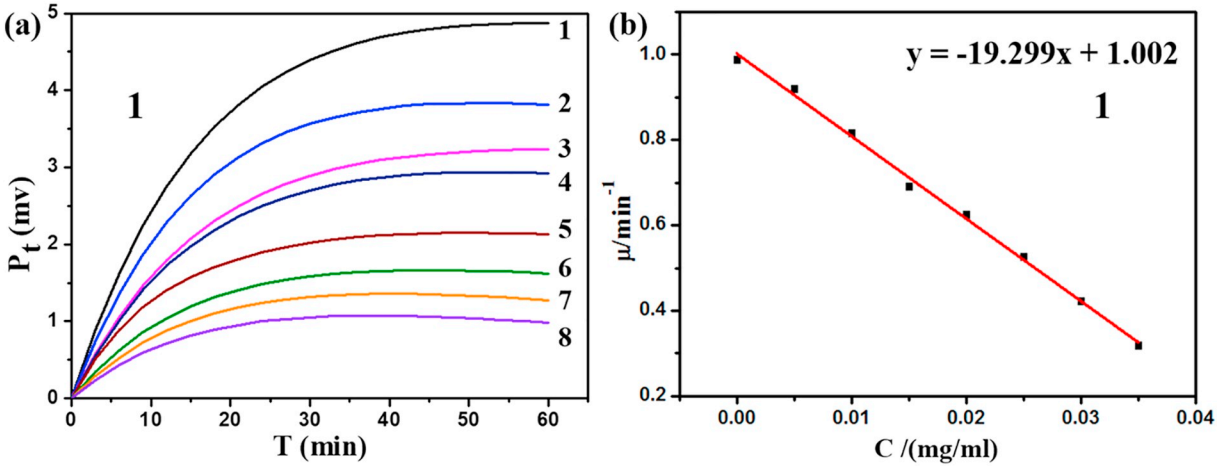

Fig. 11. (a) P_t-T curve of *E. coli* under the action of complex **1** was measured by microcalorimeter. (b) The μ-C curve of *E. coli* metabolism after incubation of complex **1**.

Table 4
The MIC (mg mL^{-1}) of target complexes and Penicillin sodium against *E. coli*.

Complex	μ-C relational	MIC(mg mL^{-1})
1	y = −19.299x + 1.002	0.05192
2	y = −18.089x + 1.076	0.05948
3	y = −12.259x + 0.777	0.06338
4	y = −15.238x + 0.840	0.05513
Penicillin sodium	y = −28.176x + 0.154	0.00547

Declaration of Competing Interest

The authors declare no competing financial interest.

Acknowledgments

We thank the University Research Development Program of Shandong Province (J18KA082), the National College Students Innovation and Entrepreneurship Training Program (2018A043), the

National Natural Science Foundation of China (Grant No. 21671118) and the Taishan Scholar Project of Shandong Province for support.

Appendix A. Supplementary data

Supplementary data to this article can be found online at https://doi.org/10.1016/j.jinorgbio.2019.110757.

References

[1] Z. Liu, P.J. Sadler, Acc. Chem. Res. 47 (2014) 1174–1185.
[2] S. Medici, M. Peana, V.M. Nurchi, J.I. Lachowicz, G. Crisponi, M.A. Zoroddu, Coord. Chem. Rev. 284 (2015) 329–350.
[3] J.M. Hearn, I. Romero-Canelon, B. Qamar, Z. Liu, I. Hands-Portman, P.J. Sadler, ACS Chem. Biol. 8 (2013) 1335–1343.
[4] P.Y. Zhang, P.J. Sadler, J. Organomet. Chem. 839 (2017) 5–14.
[5] K.Q. Qiu, H.Y. Zhu, L.N. Ji, H. Chao, Prog. Chem. 30 (2018) 1524–1533.
[6] M.D. Wang, W.H. Wang, T-S Kang, C-H Leung, D-L Ma, Anal. Chem. 88 (2016) 981–987.
[7] K.K.-W. Lo, Acc. Chem. Res. 48 (2015) 2985–2995.
[8] K.K.-W. Lo, K.K.-S. Tso, Inorg. Chem. Front. 2 (2015) 510–524.
[9] J.J. Cao, C.P. Tan, M.H. Chen, N. Wu, D.Y. Yao, X.G. Liu, L.N. Jia, Z.W. Mao, Chem. Sci. 8 (2017) 631–640.
[10] L.H. Lu, M.D. Wang, L.J. Liu, C.-H. Leung, D.L. Ma, ACS Appl. Mater. Interfaces 7 (2015) 8313–8318.
[11] H.T. Law, C.C. Lee, M.W. Louie, H.W. Liu, W.H. Ang, K.W. Lo, Inorg. Chem. 52 (2013) 13029–13041.
[12] J.P. Luzio, P.R. Pryor, N.A. Bright, Nat. Rev. Mol. Cell Biol. 8 (2007) 622–632.
[13] P. Saftig, J. Klumperman, Nat. Rev. Mol. Cell Biol. 10 (2009) 623–635.
[14] U. Repnik, B. Turk, Mitochondrion. 10 (2010) 662–669.
[15] M.E. Guicciardi, M. Leist, Gores GJ, Oncogene. 23 (2004) 2881–2890.
[16] F.X. Wang, M.H. Chen, Y.N. Lin, H. Zhang, C.P. Tan, L.N. Ji, Z.W. Mao, ACS Appl. Mater. Interfaces 9 (2017) 42471–42481.
[17] K.Q. Qiu, H.Y. Huang, B.Y. Liu, Y.K. Liu, Z.Y. Huang, Y. Chen, L.N. Ji, H. Chao, ACS Appl. Mater. Interfaces 8 (2016) 12702–12710.
[18] W.L. Ma, X.X. Ge, L.H. Guo, S.M. Zhang, J.J. Li, X.D. He, Z. Liu, Dyes Pigments 162 (2019) 385–393.
[19] L. He, Y. Li, C.P. Tan, R.R. Ye, M.H. Chen, J.J. Cao, L.N. Ji, Z.W. Mao, Chem. Sci. 6 (2015) 5409–5418.
[20] Y.L. Yang, L.H. Guo, X.X. Ge, Z.Z. Tian, Y.T. Gong, H.M. Zheng, Q. Du, X.F. Zheng, Z. Liu, Dyes Pigments 161 (2019) 119–129.
[21] T.B. Gao, R.Q. Yan, A.J. Metherell, D.K. Cao, D.J. Yeb, M.D. Ward, Dalton Trans. 46 (2017) 16787–16791.
[22] X.C. Liu, J.F. Liang, J. You, L. Ying, Y. Xiao, S.R. Wang, X.G. Li, Dyes Pigments 131 (2016) 41–48.
[23] Y. Shirota, H. Kageyama, Chem. Rev. 107 (2007) 953–1010.
[24] H.W. Zhu, F. Zhang, X.C. Liu, M.N. Sun, J.L. Han, J. You, S.R. Wang, Y. Xiao, X.G. Li, Energy Technol. 5 (2017) 1257–1264.
[25] X.M. Zhao, F. Zhang, C. Yi, D.Q. Bi, X.D. Bi, P. Wei, J. Luo, X. Liu, S. Wang, X. Li, S.M. Zakeeruddin, M. Grätzel, J. Mater. Chem. A 4 (2016) 16330–16334.
[26] F. Zhang, Z. Q. Wang, H. W. Zhu, N. Pellte, J. S. Luo, C. Yi, X. C. Liu, H. Liu, S. Wang, X. Li, Xiao Y, M. S. Zakeeruddin, D. Bi, M. Grätzel, Nano Energy. 41 (2017) 469–475.
[27] J.J. Wang, Y.M. Sun, W.J. Zhang, Y. Liu, X.Q. Yu, N. Zhang, Talanta. 129 (2014) 241–248.
[28] X.J. Ren, X.M. Lu, Q.L. Fan, W. Huang, Prog. Chem. 25 (2013) 1739–1750.
[29] W. Li, M. D. Yang, L. K. Wang, W. J. Zhu, L. N. Ye, J. Y. Wu, Y. P. Tian, H. P. Zhou, Dyes Pigments. 107 (2014) 133–139.
[30] H.B. Xiao, Y.Z. Zhang, S.Z. Li, W. Zhang, Z.Y. Han, J.J. Tan, S.Y. Zhang, J.Y. Du, Sens actuators, B. 236 (2016) 233–240.
[31] F.F. Xue, Y. Lu, Z.G. Zhou, M. Shi, Y.P. Yan, H. Yang, S.P. Yang, Organometallics. 34 (2015) 73–77.
[32] X. D. He, X. C. Liu, Y. H. Tang, J. Y. Du, M. Tian, Z. S. Xu, X. Y. Liu Z. Liu, Dyes Pigments. 160 (2019) 217–226.
[33] S.G. Fan, J. You, Y.Q. Miao, H. Wang, Q.Y. Bai, X.C. Liu, X.G. Li, S.R. Wang, Dyes Pigments 129 (2016) 34–42.
[34] X.C. Liu, F. Zhang, Z. Liu, Y. Xiao, S.R. Wang, X.G. Li, J. Mater. Chem. C 5 (2017) 11429–11435.
[35] Y. Liu, M. Nishiura, Y. Wang, Z.M. Hou, J. Am. Chem. Soc. 128 (2006) 5592–5593.
[36] Q. Zhao, F. Li, C. Huang, Chem. Soc. Rev. 39 (2010) 3007–3030.
[37] R. Cao, J.L. Jia, X.C. Ma, M. Zhou, H. Fei, J. Med. Chem. 56 (2013) 3636–3644.
[38] P. Majumdar, X.L. Yuan, S.F. Li, B.L. Guennic, J. Ma, C.S. Zhang, S.P. Yang, J. Mater. Chem. B 2 (2014) 2838–2854.
[39] M.J. Frisch, G.W. Trucks, H.B. Schlegel, G.E. Scuseria, M.A. Robb, J.R. Cheeseman, et al., Gaussian 09, revision D.01, Gaussian, Inc., Wallingford, CT, 2013.
[40] W.Z. Gao, S.R. Wang, Y. Xiao, X.G. Li, Dyes Pigments 97 (2013) 92–99.
[41] F. Bray, J. Ferlay, I. Soerjomataram, R.L. Siegel, L.A. Torre, A. Jemal, CA Cancer J. Clin. 68 (2018) 394–424.
[42] X.D. He, M. Tian, X.C. Liu, Y.H. Tang, C.F. Shao, P.W. Gong, J.F. Liu, S.M. Zhang, L.H. Guo, Z. Liu, Chem. Asian J. 13 (2018) 1500–1509.
[43] H.L. Hao, X.C. Liu, X.X. Ge, Y. Zhao, X. Tian, T. Ren, Y. Wang, C.F. Zhao, Z. Liu, J. Inorg. Biochem. 192 (2019) 52–61.
[44] Z.S. Xu, D.L. Kong, X.D. He, L.H. Guo, X.X. Ge, X.C. Liu, H.R. Zhang, J.J. Li, Y.L. Yang, Z. Liu, Inorg. Chem. Front. 5 (2018) 2100–2105.
[45] N. Sethi, Y. Kang, Nat. Rev. Cancer 11 (2011) 735–748.
[46] B.P. Espósito, R. Najjar, Coord. Chem. Rev. 232 (2002) 137–149.
[47] T. Keleş, B. Barut, Z. Biyiklioglu, A. Özel, Dyes Pigments 139 (2017) 575–586.
[48] R. Esteghamat-Panah, H. Hadadzadeh, H. Farrokhpour, J. Simpson, A. Abdolmaleki, F. Abyar, Eur. J. Med. Chem. 127 (2017) 958–971.
[49] D. Li, M. Zhu, C. Xu, B. Ji, Eur. J. Med. Chem. 46 (2011) 588–599.
[50] Y.Z. Zhang, B. Zhou, Y.X. Liu, C.X. Zhou, X.L. Ding, Y. Liu, J. Fluoresc. 18 (2008) 109–118.
[51] D.S. Raja, G. Paramaguru, N.S.P. Bhuvanesh, J.H. Reibenspies, R. Renganathan, K. Natarajan, Dalton Trans. 40 (2011) 4548–4559.
[52] A. Castiñeiras, N. Fernándezhermida, I. Garcíasantos, L. Gómez-Rodríguez, Dalton Trans. 41 (2012) 13486–13495.
[53] Z. Cheng, J. Lumin. 132 (2012) 2719–2729.
[54] J. Tang, F. Luan, X. Chen, Bioorg. Med. Chem. 14 (2006) 3210–3327.
[55] J.J. Li, X.C. Liu, H.F. Zhang, X.X. Ge, Y.H. Tang, Z.S. Xu, L.J. Tian, X.A. Yuan, X.D. Mao, Z. Liu, Inorg. Chem. 58 (2019) 1710–1718.
[56] V. Pierroz, T. Joshi, A. Leonidova, C. Mari, J Schur, I. Ott, L. Spiccia, S. Ferrari, G. Gasser, J. Am. Chem. Soc. 134 (2012) 20376–20387.
[57] C. Li, M. Yu, Y. Sun, Y. Wu, C. Huang, F. Li, J. Am. Chem. Soc. 133 (2011) 11231–11239.
[58] Z. Jing, C. Wang, G. Wang, W. Li, D. Lu, J. Sol-Gel Sci. Technol. 56 (2010) 121–127.
[59] C.L. Wang, J.F. Liu, Z.Z. Tian, M. Tian, L.J. Tian, W.Q. Zhao, Z. Liu, Dalton Trans. 46 (2017) 6870–6883.